SANDIA REPORT

SAND98–0242 • UC–405
Unlimited Release
Printed January 1998

Analysis of Gallium Arsenide Deposition in a Horizontal Chemical Vapor Deposition Reactor using Massively Parallel Computations

Andrew G. Salinger, John N. Shadid, Karen D. Devine, Harry K. Moffat

Prepared by
Sandia National Laboratories
Albuquerque, New Mexico 87185 and Livermore, California 94550

Sandia is a multiprogram laboratory operated by Sandia Corporation, a Lockheed Martin Company, for the United States Department of Energy under Contract DE-AC04-94AL85000.

Sandia National Laboratories

Issued by Sandia National Laboratories, operated for the United States Department of Energy by Sandia Corporation.

Available to DOE and DOE contractors from
Office of Scientific and Technical Information
P.O. Box 62
Oak Ridge, TN 37831

Prices available from (615) 576-8401, FTS 626-8401

Available to the public from
National Technical Information Service
U.S. Department of Commerce
5285 Port Royal Rd
Springfield, VA 22161

NTIS price codes
Printed copy: A03
Microfiche copy: A01

SAND98-0242
Unlimited Release
Printed January 1998

Distribution
Category UC-405

Analysis of Gallium Arsenide Deposition in a Horizontal Chemical Vapor Deposition Reactor using Massively Parallel Computations[1]

Andrew G. Salinger, John N. Shadid,
Scott A. Hutchinson, and Gary L. Hennigan
Parallel Computational Sciences Department

Karen D. Devine
Parallel Computer Sciences Department

Harry K. Moffat
Chemical Processing Sciences Department

Sandia National Laboratories
P.O. Box 5800
Albuquerque, NM 87185-1111

Abstract

A numerical analysis of the deposition of gallium arsenide from trimethylgallium (TMG) and arsine in a horizontal CVD reactor with tilted susceptor and a three inch diameter rotating substrate is performed. The three-dimensional model includes complete coupling between fluid mechanics, heat transfer, and species transport, and is solved using an unstructured finite element discretization on a massively parallel computer. The effects of three operating parameters (the disk rotation rate, inlet TMG fraction, and inlet velocity) and two design parameters (the tilt angle of the reactor base and the reactor width) on the growth rate and uniformity are presented. The nonlinear dependence of the growth rate uniformity on the key operating parameters is discussed in detail. Efficient and robust algorithms for massively parallel reacting flow simulations, as incorporated into our analysis code MPSalsa, make detailed analysis of this complicated system feasible.

1. This work was partially funded by the United States Department of Energy, Mathematical, Information, and Computational Sciences Division under contract no. DE-AC04-94AL85000. Sandia is a multiprogram laboratory operated by Sandia Corporation for the United States Department of Energy.

1. Introduction

In this manuscript we study a horizontal reactor with a tilted susceptor and rotating substrate that has been used for the chemical vapor deposition (CVD) of gallium arsenide (GaAs), a material used in electronic and optical devices [1-4]. A quantitative understanding of how operating and design choices effect the quality of the thin film has been difficult to achieve because of the three-dimensional geometry and the high degree of coupling between the fluid mechanics, heat transport, and species transport. Important examples include; the effect of large variations in temperature and composition on the fluid properties, the effect of thermal diffusion (the Soret effect) on mass transfer, and the existence of complex fluid motions cannot be neglected in a model that strives to be predictive [2,4].

Previous modeling efforts have made significant contributions towards an understanding of the phenomena involved in various horizontal CVD reactor configurations. These models have consisted mostly of two-dimensional models, where a slice down the center of the reactor is modeled. In a rectangular reactor (without a tilted susceptor or rotating substrate), Moffat and Jensen [5] used a parabolized approximation to the flow and transport equations to show that buoyancy forces can cause three-dimensional roll cells to develop, which seriously degrade the uniformity of the deposition in the reactor. Using an 2D model, Jansen *et al.* [1] determined that tilting the reactor only improved the uniformity moderately for systems with disk rotation. In a 2D study, Ouazzani and Rosenberger [2] found that thermal diffusion was an important transport effect, and that the 2D model agreed well with experimental results in reactors with a large width/ height aspect ratio. In a three-dimensional study, Ouazzani and Rosenberger [3] found that tilting the susceptor greatly improved the growth rate uniformity down the length of the reactor, and that side walls had a significant effect on the flow in reactors with a small aspect ratio. They also found that the choice of temperature boundary conditions on the side walls in the 3D calculations was found to have a large effect on the deposition rate distribution on the susceptor. Kleijn and Hoogendoorn [4] used 2D and 3D calculations to model the horizontal reactor, and similarly found that 2D models predicted growth rates along the center line well at conditions where roll cells do not develop, that thermal diffusion could not be neglected, and that the thermal boundary conditions at side walls have a significant effect on the predicted flow behavior.While the previous studies modeled the reaction by the transport of a single reactive species, Kleijn and Hoogendoorn [4] included multiple species and looked at the effect of different multicomponent diffusion formulations.

Due to the assumptions inherent in the 2D models and the structured grids used in the previous 3D calculations, it was not possible for previous researchers to include the effect of disk rotation on the flow. An unstructured grid is needed to mesh the circular region on the boundary.

Also, it has not previously been feasible to carry out detailed analysis of 3D models to the extent or speed where simulations are incorporated directly into the design process.

In a previous work [6], we showed how efficient utilization of massively parallel computers can enable the rapid simulation of CVD reactors, with models that include accurate representation of three-dimensional geometries through unstructured meshes, full coupling between fluid flow, heat transfer, and the transport of several species, composition-dependent physical properties, and detailed surface reaction mechanisms. The convergence to a steady-state solution from a trivial initial guess in 10-15 minutes on a portion of a parallel computer opens the door for detailed analysis of these complex models. The accuracy of the implementation of the parallel algorithms in the MPSalsa code was verified by comparison with an infinite rotating disk CVD code, SPIN [7], and the predictive capability at conditions where an accurate reaction mechanism was available was demonstrated by comparison with experimental data.

The algorithms employed in this work are described in detail in Shadid et al. [8]. A Galerkin Least Squares finite element method is used to solve the governing equations, which include the Navier-Stokes equations for incompressible, variable-density flows. All physical and transport properties vary as a function of temperature and composition, and are calculated using the Chemkin [11], Surface Chemkin [12], and Tranlib [13] libraries and thermodynamic database. A fully-coupled Newton's method is used to solve the set of nonlinear equations, with the rows of the Jacobian matrix stored fully-summed. This enables the use of domain decomposition preconditioners, such as ILU(0), to be used in the iterative linear solver (Aztec [14]) which provides the necessary robustness for the direct calculation of steady-states from a trivial initial guess.

Section 2 of this paper briefly presents the geometry, model, and numerical methods for the simulation of GaAs growth in a horizontal CVD reactor with a rotating substrate and tilted susceptor. More complete descriptions of the numerical methods and their performance are found in previous works [6, 8,15-16].

Section 3 presents results and a discussion of a series of parameter studies. First, the solution at what we have termed standard conditions is presented. Then, we show the results of five parameter studies centered around the standard conditions that give insight into the nonlinear behavior of this system. Three operating parameters and two design parameters are studied: the disk rotation rate, the inlet mole fraction of trimethylgallium (TMG), the inlet flow velocity, the amount of tilt of the reactor base, and the reactor width.

2. Model and Numerical Methods

2.1. Geometry

Figure 1 shows the reactor geometry and some surface elements of the 42721 element mesh used in this paper, which was generated by the CUBIT package [17]. The horizontal reactor is 4cm tall, 9cm wide, and 23.3cm in total length. The length includes a 4cm entrance region, and a 10cm heated susceptor region that in turn contains a 3.81cm radius disk where 3-inch diameter crystals are grown on a rotating substrate. The unstructured discretization along the reactor base allows for the resolution of the circular region inside of the rectangular domain, which will be crucial for applying boundary conditions and post-processing of the deposition rates. Two bands of smaller elements were added at the beginning and end of the susceptor region, where preliminary calculations showed that extra approximating power was needed to resolve the large gradients in the surface deposition rate.

The initial reactor design used in this paper is taken from Jansen *et al.* [1], where the base of the reactor is tilted at a 9^{o} angle after the 4cm entrance region. The mesh in Figure 1 is not tilted, because we wanted the freedom to vary the design of the reactor as a function of design parameters, including the amount of tilt. It was decided to use one standard mesh from the mesh generator, shown in Figure 1, and then for design modifications, to adjust this mesh within the parallel code using algebraic transformations that leave the connectivity between the elements unchanged. The option of using the mesh generation package to vary the reactor geometry for every change in a design parameter was not chosen because each new solution would require regenerating the mesh, re-partitioning the new mesh to run on multiple processors, and re-distributing the new mesh across all the processors. The algebraic transformation of the mesh also insures that the mesh varies continuously with the design parameters. An element quality checking routine was added to make sure that each transformation of the mesh did not create poorly formed meshes.

The transformations of the mesh are shown in Figure 2 and Figure 3. In Figure 2, three side views of the reactor and surface elements show how the tilt of the reactor is parameterized by the quantity T_R, or tilt fraction, defined as

$$T_R = \frac{\text{Reactor Height at Outlet}}{\text{Reactor Height at Inlet}} \tag{2.1}$$

which has the benefit of the constraint $0 \leq T_R < 1$, The tilt angle can be calculated from the tilt fraction by the following formula,

$$\text{Tilt Angle} = \text{atan}\left(T_R \cdot \frac{\text{Reactor Height at Inlet}}{\text{Reactor Length after Tilt}}\right), \tag{2.2}$$

where for our problem the height to length ratio is fixed at $4.0/18.3$. Tilt fractions of $T_R = 0.0$, $T_R = 0.5$, and $T_R = 0.95$ are shown in this figure. A value of $T_R = 0.725$ corresponds to the 9^o degree tilt angle that was investigated previously by Jansen *et al.* [1]. The decreasing height of the reactor down the length of the reactor when $T_R > 0.0$ causes an acceleration of the flow since the same volume of fluid must fit through a decreasing cross-sectional area. The impact of the flow acceleration on the distribution of deposition rates will be discussed in detail in Section 3.

In Figure 3, two top-views of the mesh show how the mesh can be adapted continuously to a wide range of widths. The structured rows of elements along each side of the reactor accordion to match the appropriate width, leaving the circular section free from distortion. Reactor widths of $W_R = 9.0$ and $W_R = 11.0$ are shown.

2.2. Governing Equations

The reacting flow system is governed by momentum, total mass, heat, and species mass balances. All equations are coupled together through convection, thermal diffusion, and reaction source terms as well as through the physical and transport properties, which are dependent on the local fluid composition and temperature.

The steady-state equations are shown in Table 1. The unknown variables are the three components of the velocity vector $\mathbf{u}$, the dynamic pressure P, the temperature T, and the mass fraction Y_k of each of the N_S species in the gas phase. The mixture-averaged formulation is used to model species inter-diffusion, and is written terms of the mole fractions X_k, each of which is dependent on all the species Y_k.

Except for the gravity vector $\mathbf{g}$ and the species molecular weights W_k, all of the physical and transport properties are dependent on the local values of Y_k and T. These are the density ρ, the viscosity μ, the heat capacity $\hat{C}_p$, the thermal conductivity κ, the species enthalpy h_k, the volumetric molar production rate of species k, $\dot{\omega}_k$, the mean molecular weight $\overline{W}$, the mixture-averaged diffusion coefficient D_k, and the thermal diffusion coefficient D_k^T. The values of each of these quantities is calculated using the Chemkin library [11] and Tranlib database [13]. In the momentum balance, σ is the stress tensor, the quantity I is the identity (or isotropic) tensor, and the superscript ^{T} indicates the transpose operation.

The boundary conditions for the momentum equations are as follows: plug flow inlet velocity, no normal stress boundary conditions at the outlet, counter-clockwise rotation at the rotating disk, normal flow into the reacting surface due to the surface reactions (Stefan velocity),

Momentum Balance (Navier-Stokes Eqns)	$\rho(\mathbf{u}\cdot\nabla)\mathbf{u} = \nabla\cdot\sigma+\rho\mathbf{g}$ where $\sigma = -P\mathrm{I}+\mu(\nabla\mathbf{u}+\nabla\mathbf{u}^{\mathrm{T}})-\frac{2}{3}\mu(\nabla\cdot\mathbf{u})\mathrm{I}$
Total Mass Balance (Continuity Eqn)	$\nabla\cdot(\rho\mathbf{u}) = 0$
Heat Balance	$\rho\hat{C}_p(\mathbf{u}\cdot\nabla)T = \nabla\cdot(\kappa\nabla T)-\sum_{k=1}^{N_S} h_k W_k\dot{\omega}_k$
Species Mass Balance for species k: $k = 1, \ldots, N_S-1$ Constraint on Mass Fractions: $k = N_S$	$\rho(\mathbf{u}\cdot\nabla)Y_k = \nabla\cdot\left(\frac{\rho W_k}{\overline{W}}D_k\nabla X_k\right)+\nabla\cdot\left(D_k^T\frac{\nabla T}{T}\right)+W_k\dot{\omega}_k$ $\sum_{i=1}^{N_S} Y_i = 1$

Table 1. The governing equations for steady, reacting flows of incompressible, variable density fluid. The unknown variables are the three components of the velocity vector $\mathbf{u}$*, the dynamic pressure* P*, the temperature* T*, and the mass fraction* Y_k *of each of the* N_S *species in the gas phase.*

and no-slip, no-penetration conditions everywhere else. The heat equation has boundary conditions of $T = 300K$ at the reactor inlet, $T = 913K$ on the susceptor, $T = 675K$ on the top wall directly above the susceptor. In the quartz, the temperature was fixed at

$$T = 913 - 238(1 - e^{-1.25y}), \tag{2.3}$$

which is a fit to the profile given in Figure 3 of Jansen *et al.* [1], after being adjusted to a 913K susceptor temperature (where y is the distance from the susceptor). All other walls are modeled as adiabatic. The mass transfer boundary conditions fix the inlet mole fractions at the inlet, match the flux at the reacting susceptor to the surface reaction rate (see following section), and specify no normal diffusive flux at all other boundaries.

2.3. Chemistry Model

The chemistry model from Moffat *et al.* [23] for the deposition of galliumarsenide ($GaAs$) from trimethylgallium (TMG or $GaMe_3$) and arsine (AsH_3) in excess hydrogen (H_2) is used. This mechanism involves four gas phase species, $GaMe_3$, AsH_3, H_2, and methane (CH_4), which is produced at the reactive surface.

This model does not include any gas phase reactions, but does include four surface reactions shown in Table 2. The mechanism includes inhibition of the surface reactions due to a

blocking effect of the adsorbed Arsine. The stoichiometry only allows for equal deposition rates of solid Gallium and Arsenide, so no impurities can be predicted. The mechanism was fit using data collected in a rotating disk reactor at a pressure of 70 torr and a surface temperature of 640C -- and is not necessarily accurate at other conditions -- so these parameters were not varied in the following analysis. We have compared calculations of deposition rates in the rotating disk reactor using this mechanism with experimental data and found excellent agreement [6].

Three surface species (denoted by the -(S) suffix in Table 2) are included in the model and their surface site fractions are solved for using a quasi-steady approximation. By assuming that the surface reactions equilibrate much faster than any changes in the gas phase, the surface fractions can be solved for as a function of the gas phase concentrations and eliminated as unknowns from the problem. This entails the solution of a small nonlinear system at every surface node, at every Newton iteration, and at every new parameter value in the analysis. It has been shown that this adds robustness over the option of solving for the surface site fractions of surface species simultaneous with the global unknowns [25].

Surface Reactions	A or k	E_a cal/mole
$AsH_2(S) + GaMe_3 \Rightarrow 2CH_4 + As(D) + GaMe(S)$	$A = 0.015$	0
$AsH_2(S) + AsH_3 \Rightarrow Block(S)$	$A = 0.37$	9000.
$Block(S) \Rightarrow AsH_2(S) + AsH_3$	$k = 10^{13}$	44000.
$GaMe(S) + AsH_3 \Rightarrow CH_4 + Ga(D) + AsH_2(S)$	$A = 0.20$	0

Table 2. Surface reaction mechanism for the deposition of $GaAs$ from $GaMe_3$ and AsH_3, including surface inhibition. Reaction rates expressed in terms of a sticking coefficient A or an Arrhenius pre-exponential factor k [7]

2.4. Numerical Methods

A large investment has been made into developing efficient and robust methods for modeling chemically reacting flows on massively parallel computers. This work has been incorporated into the MPSalsa reacting flows code and the Aztec linear solver package. Only a brief overview will be included here. Shadid *et al.* [8] contains a detailed description of the equations, finite element method, and parallel implementation in MPSalsa. Details on the methods in Aztec can be found in [14]. Performance of the algorithms on some model problems has been detailed in earlier papers [9, 10, 16]. Benchmarking of the solution against other codes and experimental data can be found in Salinger *et al.* [6, 15].

The governing equations in Table 1 are discretized using a Petrov-Galerkin finite element method. The domain is divided into an unstructured mesh of hexahedral elements using the CUBIT mesh generation package[17]. All variables are approximated by trilinear basis functions within each element. The equal-order interpolation of pressure and velocity unknowns is enabled by a Galerkin Least Squares stabilization formulation [18, 19], which adds a term to the continuity equation that vanishes for any solution that satisfies Navier-Stokes equations.

To solve the model on P processors, the nodes of the mesh are partitioned into P equal subsets using Chaco [20, 21], a generalized graph partitioning package. Each processor is then assigned its own subset of the mesh without any processor having a knowledge of the complete domain. A processor calculates the finite element residuals and rows of the Jacobian matrix (or sensitivities) only for the nodes that it owns. The partitioner assigns equal numbers of FE nodes to each processor to balance the computational load. In addition, the partitioner attempts to minimize the amount of interprocessor communication needed to calculate the FE residuals and other connectivity (mesh) based calculations. For the solutions presented in this paper we used 512 processors of the 1840 processor Intel Paragon located at Sandia National Labs.

Newton's method is used to solve the resulting set of nonlinear residual equations. With the 42621 element mesh shown in Figure 1 and the four-species chemistry mechanism written in Table 2 (which contributes to a total of 9 unknowns per node), the finite element discretization creates a set of 423468 coupled nonlinear equations and unknowns. The Jacobian matrix is calculated analytically for all terms except for those pertaining to the gas and surface reactions, which are calculated numerically using a simple one-sided difference. The dependence of the physical properties on the solution is handled by successive substitution in the calculation of the Jacobian matrix (except for the temperature dependence of the density in the buoyancy term which is explicitly include in the Jacobian). This choice can increase the number of Newton iterations needed for convergence of the nonlinear problem over what one would find with an exact Jacobian when solving non-dilute problems. However, for the dilute problems presented here this is a very efficient choice.

In the simulations presented in this paper each iteration of Newton's method requires the solution of a matrix problem of 423468 linear equations and unknowns, for which we use the Aztec library of preconditioned Krylov methods [14]. In our solution method we row sum scale our matrices and use an overlapped Schwarz domain decomposition method with an ILU(0) subdomain preconditioner. The restarted GMRES iterative method [22] was used with a Krylov subspace size of 150 and one restart allowed (for a maximum of 300 linear solver iterations). The linear solver was required to reduce the scaled residual by a factor of 0.004 at each Newton step.

With the combination of Newton's method and the preconditioned linear solver, it was always possible to reach a steady-state solution directly from a trivial initial guess or from a previous solution at different conditions. This would not be the case if a simpler preconditioner was used, such as block-Jacobi method [14], or if the Krylov subspace size for the GMRES method was greatly reduced, perhaps below 50. If the advanced solution algorithms available in the Aztec library [14] and the large computer memory of our parallel machine were not available for this robust methodology, a steady-state solution would have to be reached through time-integration. This transient process would likely take 10-100 times longer and make detailed analysis impractical.

3. Parameter Study Results

3.1. Solution at Standard Conditions

Table 3 lists many of the operating and design parameters that can be independently varied in the horizontal CVD growth of $GaAs$. Reasonable values of the parameters, which we will call the standard conditions, are shown. For the five parameters whose influence is investigated in this work, the ranges over which they are varied are also indicated. The standard values of the design parameters come from Jansen et al. [1], the work that also guided our choices for the inlet velocity, inlet temperature, and inlet mole fraction of trimethylgallium. The operating temperature and pressure are fixed at the values where the reaction mechanism in Table 2 is valid [23], and the arsine to trimethylgallium ratio was held fixed at 10 [24].

The disk rotation rate of 50rpm was chosen to be fast enough so that the length of time for a typical growth run would be much larger than the period of revolution, which exposes each sector of the disk to the same conditions. This assumption that the rotation period is fast compared to the growth run together with the quasi-steady assumption that the surface reactions are fast compared to the disk rotation rate, allow us to reduce the two-dimensional instantaneous deposition rates over the disk to a one-dimensional, time-averaged radial deposition profile by integrating over the azimuthal coordinate θ. That is, any point on the disk at a given radius will experience the same deposition over an entire growth run as any other point on the disk at the same radius, so the time-averaged growth rate at that radius can be calculated by the spatial average of the instantaneous growth rate of all points at that given radius.

The calculation started from a trivial initial guess and reached a steady-state in 13 Newton iterations. This number is larger than one might expect for Newton's method for two reasons. First, the variation of the physical and transport properties with respect to the local temperature and vector of mass fractions was not included in the Jacobian (a.k.a. stiffness) matrix. Secondly,

Parameter	Description [units]	Standard Value	Range
Ω	Substrate (Disk) Spin Rate [rpm]	50	0-500
X	Inlet Mole Fraction of TMG	0.00010	0.00005-0.00020
V	Inlet Flow Velocity [cm/sec]	40	10-100
T_R	Tilt Fraction of Reactor Base	0.725	0.0-0.95
W_R	Reactor Width [cm]	9.0	8.7-13.0
H_R	Reactor Height [cm]	4.0	
R	Substrate (Disk) Radius [cm]	3.81	
T_{In}	Inlet Reactor Temperature [K]	298	
T_H	Susceptor Temperature [K]	913	
X_{AsH3}	Inlet Mole Fraction of Arsine	$10 \times X$	
P	Reactor Pressure [torr]	70	

Table 3. List of operating and design parameters for the deposition of $GaAs$ in a horizontal CVD reactor with tilted susceptor and rotating substrate. The "standard" conditions are listed, as well as ranges for parameters that are varied in this work.

the iterative linear solver was only required to reduce the linear residual by 4.0e-3, and not down to zero as a direct solver would do. It has been found that setting this criterion rather loose, so that the linear solver exits relatively soon at each Newton iteration (a technique called an Inexact Newton method), can greatly reduce the total CPU time needed to reach a solution, even though the number of Newton iterations is usually increased [10].

The time for MPSalsa to calculate the finite element residual equations and Jacobian matrix was 11 seconds for each Newton iteration, while the linear solution time (in Aztec [14]) for each Newton step had a range of 16-64 seconds. The total computational time to steady-state, neglecting the I/O time, was 10 minutes. This robustness and short turn around time for solving three-dimensional flow coupled with reactions make detailed analysis of this reactor feasible. The following five sections use continuation method to investigate the effect of several key operating and design parameters on the performance of the reactor.

Both the time-averaged radial deposition profile over the rotating disk and the instantaneous deposition contours over the entire susceptor, which includes the disk, are shown in Figure 4, which were calculated at the standard conditions. The deposition contours show very large deposition at the leading edge of the disk. Also noteworthy is the slight left-right asymmetry due to the counterclockwise rotation of the disk.

The radial profile shows that the deposition rate is not very uniform, with a 6% drop in the deposition rate from the center to the outer edge. The deposition contours show that the deposition is fairly uniform along the flow direction, but there is decreased deposition at the edge of the disk is due to the slow rates at the left and right sides of the reactor. The momentum boundary layer from drag on the side walls, by decreasing the flow rate, also increases the size of the boundary layer between the bulk fluid and the reactive bottom of the disk. This increase in mass transfer resistance causes the decrease in deposition rates and the resulting non-uniformity of the growth.

Since Figure 4 indicates that the bulk of the non-uniformity of the deposition rate is due to the momentum boundary layers at the side walls, it would be expected that changes in at least two parameters could be made to improve the performance of the reactor. One would be to alter the design of the reactor to make it wider while keeping the disk radius constant, so that the boundary layer is moved off of the disk. The second would be to increase the gas velocity through the reactor to shrink the boundary layer so that less of it effects the disk. These changes will be investigated in subsequent sections.

3.2. Disk Spin Rate, Ω

The effect of the disk (or substrate) rotation on the deposition rate and uniformity is investigated in this section. With all other parameters fixed at the standard values of Table 3, the disk spin rate was varied from 0 - 500 rpm in increments of 100. Simple zero-order continuation was used, so that the solution at 0 rpm was used as an initial guess for the solution at 100rpm, and so on. This reduced the number of Newton iteration needed to reach the solution to 8-10, as compared to the 13 seen in Section 3.1 when starting from a trivial initial guess. Also, the loading in of the mesh and load balance information needed to be done just once for the entire continuation run, and it was not necessary to repeatedly wait for the 512 processors to become available. The entire run required 40 minutes.

The result of the parameter study on the disk spin rate Ω is summarized in Figure 5. As a single measure of the solution we use the deviation from uniform growth of the time-averaged deposition on the disk (which is a function of radial position only), defined as

$$\text{Non-Uniformity} = \frac{\text{Max Deposition Rate} - \text{Min Deposition Rate}}{\text{Average Deposition Rate}}. \tag{3.1}$$

Figure 5a shows that the non-uniformity deteriorates monotonically from 5.9% at $\Omega = 0$ to 6.4% at $\Omega = 500$. (The $\Omega = 0$ result should be thought of as a limit, since this would violate our assumption used in time-averaging the deposition rates that the period of revolution is fast

compared to the time for the entire growth run. If there truly was no disk rotation and therefore no time-averaging of the deposition profiles, the non-uniformity would be about 25% .)

The radial or time-averaged deposition profiles in Figure 5b show that the disk rotation increases the deposition at the center of the disk while not significantly effecting the deposition rate at the edge of the disk. Since the center of the disk already exhibited a higher growth rate than the edge, this increase causes a corresponding increase in the non-uniformity. Figure 5c-e show instantaneous contours of the deposition rate at three values of the spin rate. The spinning disk distorts the deposition profiles from the symmetric contours when there is no spinning.

It is not clear from the three contour profiles what mechanism causes the increase in deposition at the center of the disk. One possible explanation is that the rotation of the disk causes a slight swirling and mixing in the flow, which pulls in reactant from the sides of the reactor where they are not as depleted as in the center, further increasing the growth rate at the center.

Since this parameter study suggests that increasing disk rotation over the minimum needed to time-average the deposition degrades the uniformity of deposition, a fixed value of $\Omega = 50$ is used in subsequent parameter and ongoing optimization studies.

3.3. TMG Mole Fraction, X

The second parameter study involves the inlet mole fraction of the limiting reactant, trimethylgallium, X, which is varied in the range of $0.00005–0.00020$. The other parameters are fixed at the standard conditions listed in Table 3, including the inlet mole fraction of arsine (X_{AsH3}) which floats at ten times the mole fraction of TMG. The zero-order continuation run consists of 16 steady-state calculations, which required about 100 minutes on 512 processors of the Intel Paragon.

Figure 6 summarizes the results of this study. The plot of the Non-Uniformity of the solution (defined in Eqn. (3.1)) in Figure 6a shows that the there is a weak dependence of the quality of deposition on X, with slightly better uniformity at higher inlet mole fractions. Three radial deposition profiles at evenly spaced parameter values show that X has a large impact on the magnitude of deposition. It also appears from this figure that the dependence is nearly linear.

The linear dependence of the growth rate on X is verified by looking at the instantaneous deposition rate contours shown in Figure 6c-e. Notice how the 3.0, 3.5, and 4.0 contours at $X = 0.00006$ line up almost exactly with the 6.0, 7.0, and 8.0 contours at $X = 0.00012$ and the 9.0, 10.5, and 12.0 contours at $X = 0.00018$. It is not clear from either the time-averaged radial deposition profiles or the instantaneous deposition contours why increasing X slightly

improves the overall uniformity of the growth, but it must be a nonlinear transport effect such as the dependence of the diffusion coefficients on the composition.

The nearly linear dependence on X is expected since the deposition process is highly mass-transfer limited. This is in part built into the reaction mechanism, which does not include any gas phase reactions.

3.4. Inlet Velocity, V

The third and final operating parameter studied is the inlet velocity of the gases into the reactor. The inlet velocity is assumed plug flow and the gas perfectly well mixed, which is a reasonable approximation if the gas is forced to flow through a screen placed at the inlet to our computational regime. The parameter study involved 17 steady state calculations for inlet velocities in the range of $10 - 100$ cm/sec, with all other parameters set at the standard conditions from Table 3. The entire run required about 130 minutes on 512 processors of the Intel Paragon.

The results showing the effect of the inlet velocity on the reactor performance are summarized in Figure 7. The continuation run is shown in Figure 7a, using the non-uniformity of the deposition rate over the disk (Eqn. (3.1)) as the measure of the solution. A highly non-linear effect is seen, with a maximum non-uniformity of 6.9% at $V = 30$, a minimum of 1.3% at $V = 68$, a steadily rising up to 4.2% non-uniformity at $V = 100$.

The time-averaged radial deposition profiles in Figure 7b show that the deposition rate increases with increasing velocity. The mechanism for this is that faster flow causes a thinner boundary layer along the base of the reactor, and therefore less resistance to mass transfer to the surface. The deposition profiles switch from monotonically decreasing with radius at low flow rates to monotonically increasing at high flow rates. In other words, the non-uniformity of the deposition at low flow rates is due to slower deposition at the edge of the disk than at the center, while at high flow rates it is due to faster deposition at the edge than at the center. The best solution occurs at $V = 68$, where the center and edge are growing at the same rate. The jump in the position of the minimum deposition rate from the edge to the center explains the discontinuity in slope of the non-uniformity at $V = 68$ in Figure 7a.

To understand why the radial deposition profiles switch from decreasing with radius to increasing with radius as the flow rate increases, and thereby understanding the nonlinear phenomenon in Figure 7a, we look at the instantaneous deposition contours over the susceptor, Figure 7c-e. At the slower flow rate, $V = 30$, we see that there are large sections of the left and right edges of the disk that deposition rates below 5.0 Angstroms/sec. This is due to the large boundary layer forming at the left and right walls of the reactor, that slow down the flow and

decrease mass transport to the surface. This effect is not captured in 2D models. These regions of low deposition rates compared to the center of the disk are partially balanced (when all deposition rates at the same radius are averaged) by a deposition rate at the leading edge of the disk that is much higher than that at the center, reaching 6.5 Angstroms/sec. Overall, the effect of the side walls dominate and a 6.9% decrease in deposition is seen, which is unacceptable performance for most applications.

If we jump to Figure 7e which shows the deposition contours at the highest flow speed investigate, $V = 100$, we can see why the $V = 100$ deposition profile in Figure 7b increased with increasing radius. First of all, the higher flow rate has condensed the boundary layers along the left and right side walls, so that this effect which dominated at $V = 30$ is much smaller. Most notable in this figure is the large area at the back, or downstream edge of the disk (the upper part with the orientation of our figures) where the deposition rate is above 7.0 Angstroms/sec. It is this large area of elevated deposition rate, along with the smaller contribution at the leading edge of the disk, which causes the deposition rate a larger radii to be faster than that at the center.

The mechanism responsible for this elevated deposition rate is believed to be the interplay between two competitive effects. The first is the depletion of the reactant, which alone would cause the deposition rate to decrease down the length of the reactor. The second mechanism is the acceleration of the fluid flow down the length of the reactor due to the tilted base, which increases the flow rate above the back edge of the disk, which decreases the mass transfer resistance to the surface, and therefore would alone increase the deposition rate down the length of the disk. Ideally, one would like these two effects to cancel, but in Figure 7c-e we can see that increasing the flow rate tips the balance toward the second (flow-acceleration) mechanism, so at $V = 100$ the deposition at the back end of the disk is significantly faster than at the center of the disk.

This finally brings us to Figure 7d at $V = 68$, which exhibits the most uniform growth. We can see that this local optimum strikes a balance between the $V = 30$ and $V = 100$ cases. There is still significant decreases in deposition rate along the left and right edges of the disk, due to the boundary layers developed at the side walls. There is also a significant increase in the deposition rate at the back end of the disk due to flow acceleration. At this flow rate, these two effects balance and the deposition rate at the center of the disk is exactly the same as the averaged deposition rate at the edge of the disk (6.4 Angstroms/sec), as can be seen in Figure 7b.

From our studies of three operating parameters, operating the reactor at $V = 68$ cm/sec, while fixing other parameters at the standard values, appear to be the best conditions for this given reactor. However, the deposition contours in Figure 7d have shown that the superior uniformity at these conditions is the result of a precarious balance between one effect that slows deposition towards the edge of the disk and another that accelerates it. This is reflected in the relatively steep

slopes of the curve on either side of the minimum in Figure 7a. A sensitivity analysis around this solution to account for some of the uncertainties in the physical, transport, and reaction parameters would likely show a similar steep degradation of uniformity as parameters were perturbed around this local optimum.

3.5. Tilt of Reactor Base, T_R

To further decrease the non-uniformity of deposition to values below the 1.3% value located by varying operating parameters, alterations in the design of the reactor are investigated. By allowing the reactor geometry to deform continuously in terms of a parameter, design studies can be performed in the same way as the operating studies above. As discussed in Section 2.1, we chose to alter the finite element mesh within MPSalsa, in parallel, instead of through the mesh generator, in serial. This significantly reduced computation time and insured that the mesh variation was indeed continuous with respect to the design parameters -- which could not be guaranteed when using the mesh generator.

The first design parameter studied is the tilt fraction of the mesh, defined in Eqn. (2.1), which can be related to the tilt angle through Eqn. (2.2). The standard value of the tilt fraction in this work, that has been used in all previous calculations, was $T_R = 0.725$, which corresponds to the 9° tilt angle used in Jansen *et al.* [1]. A parameter study involving 14 calculations at distinct values of T_R in the range of 0.0–0.95 was performed using the zero-order continuation routine, and required 90 minutes on 512 processors of the Intel Paragon.

The results of the parameter study are summarized in Figure 8. Figure 8a shows that the non-uniformity, as defined in Eqn. (3.1), increases from a value of 5.8% at $T_R = 0.0$ to a maximum of 6.2% at $T_R = 0.5$, and then decreases to 4.2% at $T_R = 0.95$, the best solution achieved in this run. The time-averaged radial deposition profiles in Figure 8b show that the tilt fraction can have a large effect on the magnitude of the deposition, with the deposition at the center of the rotating disk increasing from 4.3 Angstroms/sec at $T_R = 0.0$ to 6.9 Angstroms/sec at $T_R = 0.95$. This deposition increase is due to the acceleration in the flow velocity over the disk that accompanies the decreased cross-sectional area of the reactor when the tilt is increased. These radial profiles do not add insight into the nonlinear dependence of the tilt fraction on the overall uniformity, as seen in Figure 8a.

Instantaneous deposition contours at $T_R = 0.0$, $T_R = 0.5$, and $T_R = 0.95$ are shown in Figure 8c-e, and the solution at $T_R = 0.725$ was shown in Figure 4. It can be seen that all deposition profiles are effected by the boundary layers that decrease deposition on the on the left and right edges of the rotating disk. If one looks just at the deposition along the centerline of the reactor, which is vertical in these plots, the competition between the reactant depletion and flow

acceleration mechanisms, as discussed in Section 3.4, can be clearly seen. In the case of no tilt, the effect of reactant depletion is evident, with the deposition dropping from almost 6.0 at the front of the disk to about 3.8 at the back. At $T_R = 0.5$, the deposition still drops along the length of the reactor, but not as much as the previous case. This is because the flow acceleration mechanism for increasing deposition along the length of the reactor is partly balancing the reaction depletion mechanism. At $T_R = 0.95$, the flow acceleration mechanism dominates and the deposition increases greatly down the reactor, reaching a rate of 8.0 at the back of the disk. The two mechanisms are well balanced at $T_R = 0.725$, shown in Figure 4, with no contours crossing the disk centerline except in the transition region at the front of the disk. As we saw in the previous section, these results are highly dependent on the inlet flow velocity, which is fixed at $V = 40$ in this section.

Even thought the best uniformity is seen at the maximum tilt fraction studied, $T_R = 0.95$, this is due to averaging of low deposition rates at the sides of the disk and high deposition rates at the back of the disk. The solutions at the standard value of $T_R = 0.725$ would appear to be a better choice for this flow velocity if the effects of the boundary layers on the sides of the reactor could be diminished.

3.6. Reactor Width, W_R

The second design parameter studied is the reactor width, which was fixed at $W_R = 9.0\,\text{cm}$ in all the previous calculations. The need to increase the width of this reactor design is evident from any of the above plots showing instantaneous deposition contours over the susceptor, including at standard conditions in Figure 4. It is expected that increasing the reactor width will move the momentum boundary layer at the side wall and associated region of decreased deposition rate off the edge of the disk, thereby improving the uniformity of growth.

A continuation run of 18 steady-state calculations for reactor widths in the range of 8.7 – 13.0 cm were calculated in about 100 minutes on 512 processors of the Intel Paragon. The results are summarized in Figure 9. Figure 9a show the non-uniformity of deposition decrease from 7.0% at $W_R = 8.7$, down to a minimum of 0.2% at $W_R = 11.3$, and then rising to 2.1% at $W_R = 13.0$.

Figure 9b shows the time-averaged radial profiles for three of the solutions. The profiles clearly switch from concave down at small widths ($W_R = 9.0$), through a nearly flat profile at $W_R = 11.3$, to concave up deposition profiles at larger widths ($W_R = 13.0$). The average deposition rate varies little as a function of the reactor width.

The instantaneous deposition contours over the susceptor for the same three widths are shown in Figure 9c-e. As expected, the region of decreased deposition along the two sides of the reactor move off the edge of the disk as the reactor width is increased. The most uniform solution of this continuation run, at $W_R = 11.3$, is again (like the solution at $V = 68$ in Section 3.4) a balance between below-average deposition rates at the sides of the disk and above-average deposition at the leading and back ends of the disk; however, the instantaneous profiles are much more uniform in this case than in velocity run, so this solution is not in as precarious a spot in parameter space.

Of all the solutions seen in the parameters studies, the solution at $W_R = 13.0$ shows the least effect of the side walls on the deposition rate on the disk and has by far the largest disk area with the deposition rate falling between two contour values. The average deposition rate for this reactor shows an increase of deposition at large radii because of the increased deposition at the leading edge and, to a lesser extent, the back end of the disk. From the earlier studies, on can see that lowering the velocity might lower the deposition rate preferentially in these two areas. Decreasing the tilt angle, and therefore the acceleration of flow through the reactor, would lower the deposition rate at the back edge of the disk, pushing the 6.0 contour off the edge of the disk. Through manipulations such as these, one can see how it should be possible to come up with conditions where the model predicts even better solutions than the 0.2% non-uniformity solution seen so far. Optimization is a way to automate the process of manipulating multiple parameters to locate the best possible conditions as predicted by the model, and is the subject of ongoing work.

4. Summary and Conclusions

The MPSalsa reacting flows code has been used to analyze a three-dimensional model of GaAs deposition in a horizontal CVD reactor that includes coupled flow, heat transfer, and chemistry. A series of parameter studies on five key operating and design parameters have been performed with a focus on how each parameter effects the uniformity of deposition over a three-inch diameter spinning substrate. The effect of the parameters on the uniformity, which was often nonlinear, was investigated in detail through contour plots of deposition rates. The most notable result was that a significant increase in the reactor width could alone lead to deposition non-uniformities of as low as 0.2%.

In this study we have shown that using advanced numerical methods and parallel computing technology has enabled a detailed analysis of this complex 3D CVD reactor with exceptionally low turnaround time. This capability is critical to the detailed analysis of these complex systems where often many operating and design parameters have competing influences. We have also shown that a 3D model is needed to capture all the behavior in the reactor and for

creating an improved understanding of the many transport effects in the reactor. In our study we were able to demonstrate a 30x improvement in deposition rates for our reactor model. While as discussed earlier there are some limitations to the predictability of our model we believe these results are reasonable and do demonstrate the usefulness of our techniques. As more well documented and predictive kinetics models become available, analyses such as these can furnish results with more confidence.

Our analysis study has shown that there is a significant potential benefit from computational studies of CVD systems. We believe the next challenge is to use a computational optimization technique to solve the real engineering objectives associated with CVD reactor design and operation. These objectives can include achieving high uniformity while keeping raw materials costs down to maximize profits for a particular reactor. This goal can only be met by simulation methods which provide robustness, high computational efficiency and model predictability.

References

1. A.N. Jansen, M.E. Orazem, B.A. Fox, and W.A. Jesser, J. Crystal Growth, 112, (1991) 316-336.
2. J. Ouazzani, K.-C. Chiu, and F. Rosenberger, J. Crystal Growth, 91, (1988) 497-508.
3. J. Ouazzani and F. Rosenberger, J. Crystal Growth, 100, (1990) 545-576.
4. C.R. Kleijn and C.J. Hoogendoorn, Chem. Eng. Sci., 46(1) (1991) 321-334.
5. H.K. Moffat and K.F. Jensen, J. Electrochem. Soc., 135 (1988), 459.
6. A.G. Salinger, J. N. Shadid, H. K. Moffat, S. A. Hutchinson, G. L. Hennigan, K. D. Devine, submitted as Sandia National Laboratories Technical Report (1997).
7. M. E. Coltrin, F. J. Kee, G. H. Evans, E. Meeks, F. M. Rupley, and J. F. Grcar, Sandia National Laboratories Technical Report, SAND87–8248 (1987).
8. J. N. Shadid, H. K. Moffat, S. A. Hutchinson, G. L. Hennigan, K. D. Devine, and A. G. Salinger, Sandia National Laboratories Technical Report, SAND95–2752 (1996).
9. J. N. Shadid, S. A. Hutchinson, G. L. Hennigan, H. K. Moffat, K. D. Devine, A. G. Salinger, To be published in special issue of Parallel Computing on flow simulations (1997).
10. J. N. Shadid, R. S. Tuminaro, H. F. Walker, "An inexact Newton method for fully-coupled solution of the Navier--Stokes equations with heat and mass transport", To be published in J. Comp. Phys (1997).
11. R. J. Kee, F. M. Rupley, E. Meeks, and J. A. Miller, Sandia National Laboratories Technical Report, SAND96–8215 (1996).
12. M. E. Coltrin, R. J. Kee, and F. M. Rupley, E. Meeks, Sandia National Laboratories Technical Report, SAND96-8217 (1996).
13. R. J. Kee, G. Dixon-Lewis, J. Warnatz, M. E. Coltrin, J. A. Miller, Sandia National Laboratories Technical Report, SAND86–8246 (1986).
14. S. A. Hutchinson, J. N. Shadid and R. S. Tuminaro, Sandia National Laboratories Technical Report, SAND95–1559 (1995).
15. A.G. Salinger, K.D. Devine, G.L. Hennigan, H.K. Moffat, S.A. Hutchinson, and J.N. Shadid, Sandia National Laboratories Technical Report, SAND96-2331 (1996).
16. J. N. Shadid, S. A. Hutchinson, H. K. Moffat, G. L. Hennigan, B. A. Hendrickson, and R. W. Leland, Proceedings of Supercomputing '94, Washington, DC, Nov. 14–18, (1994) 673–679.
17. T. D. Blacker et al., Sandia National Laboratories Technical Report, SAND94–1100, May (1994).
18. T. J. R. Hughes, L. P. Franca, M. Balestra, Comp. Meth. App. Mech. and Eng., 59, (1986) 85–99.
19. T. E. Tezduyar, Advances in App. Mech., 28, (1992) 1–44.
20. B. Hendrickson and R. Leland. Proceedings of Supercomputing '95, ACM, November (1995).

21. B. Hendrickson and R. Leland, Sandia National Laboratories Technical Report, SAND94-2692 (1995).
22. Y. Saad and M.H. Schultz, SIAM J. Sci. Stat. Conp., 7(3), (1986) 856-859.
23. H. K. Moffat, K. P. Killeen, and K. C. Baucom, (1995) submitted.
24. W. G. Breiland and H.K Moffat, (1996) private communication
25. R. Venkataramani, H.K. Moffat, A.G. Salinger, (1996) in preparation.

Figure 1. Surface elements of the 42721 element mesh show the geometry of the horizontal CVD reactor in the case where the base is not tilted. Following the specifications in Jansen et al. [1], the total length of the reactor is 23.3cm, the height is 4cm, and the width is 9cm. The unstructured mesh resolves the 3-inch diameter disk (substrate), which is inset in the susceptor, for accuracy in applying boundary conditions and in post-processing.

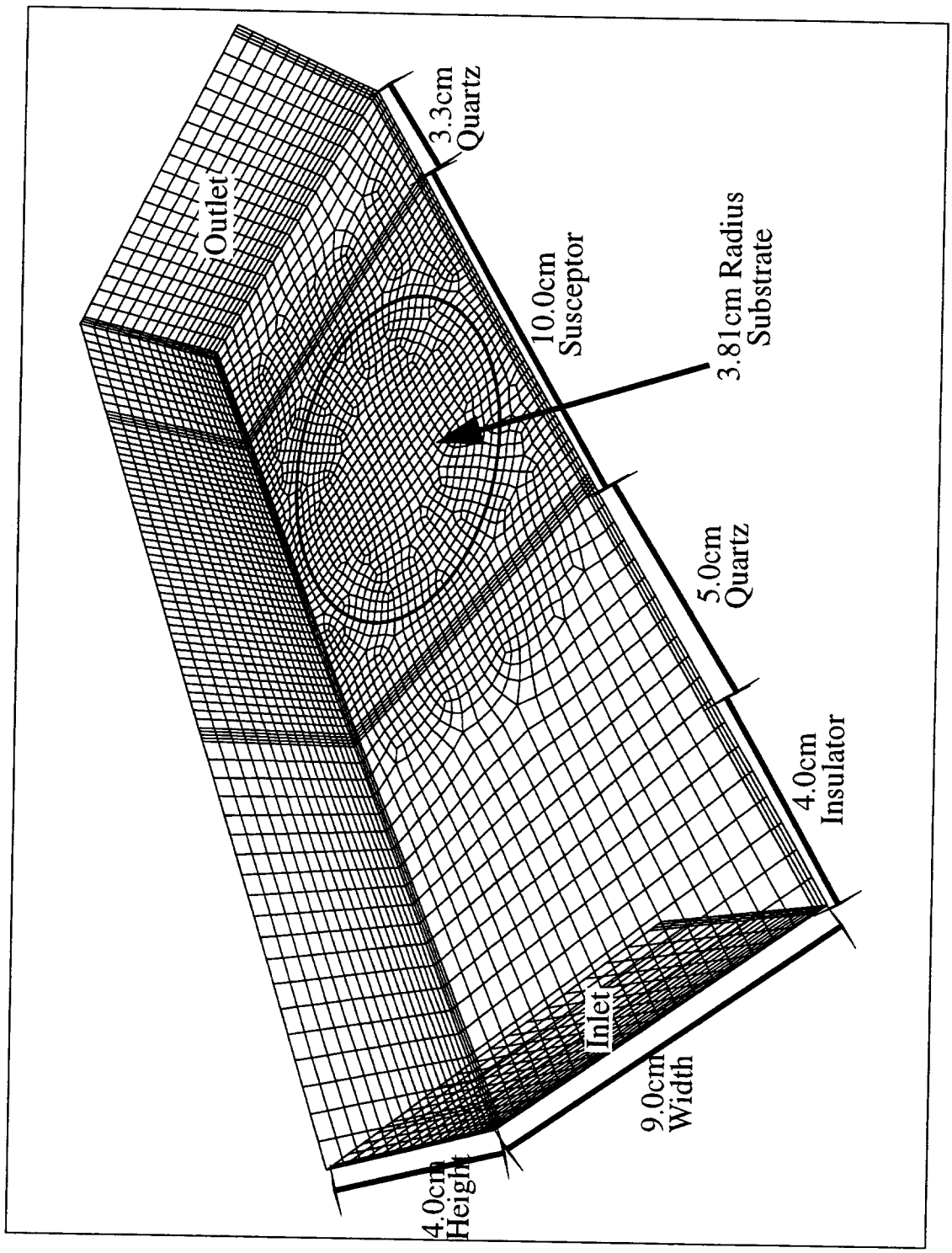

Figure 2. Three side-views of the reactor and mesh show the effect of T_R, the design parameter representing the tilt fraction of the mesh. When $T_R = 0.0$, the mesh is rectangular, at $T_R = 0.50$, half the outlet is constricted, and at $T_R = 0.95$, the outlet is only 5% of the original height. A value of $T_R = 0.725$, not shown, corresponds to a tilt angle of 9°, which was used in previous work [1].

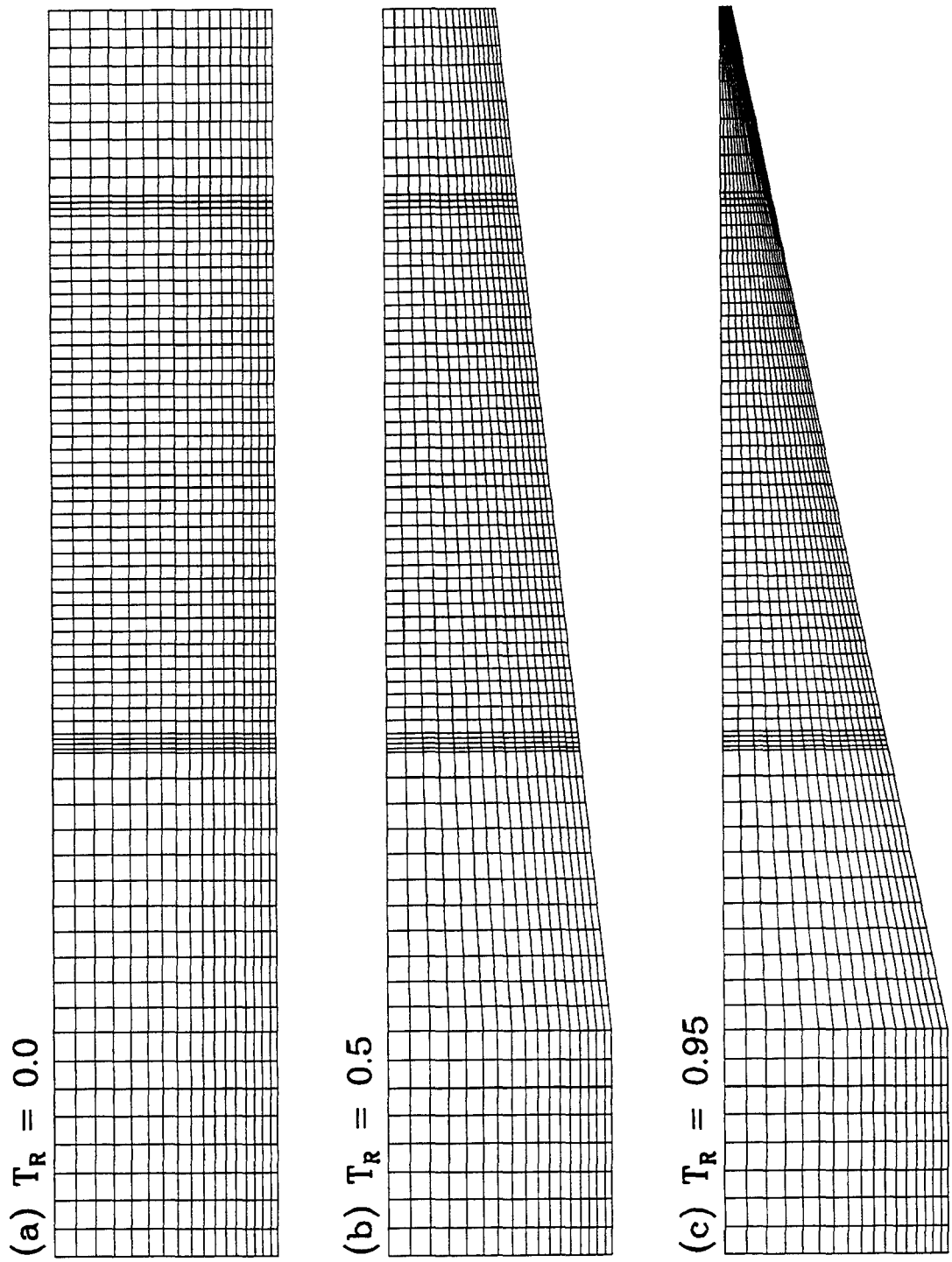

Figure 3. Two top-views of the mesh show the effect of W_R, the design parameter representing the width of the reactor in centimeters. A structured region of the mesh on each side of the mesh was created to simplify this parameterization. The value of $W_R = 9.0$ was used in the experimental set-up of a previous work [1].

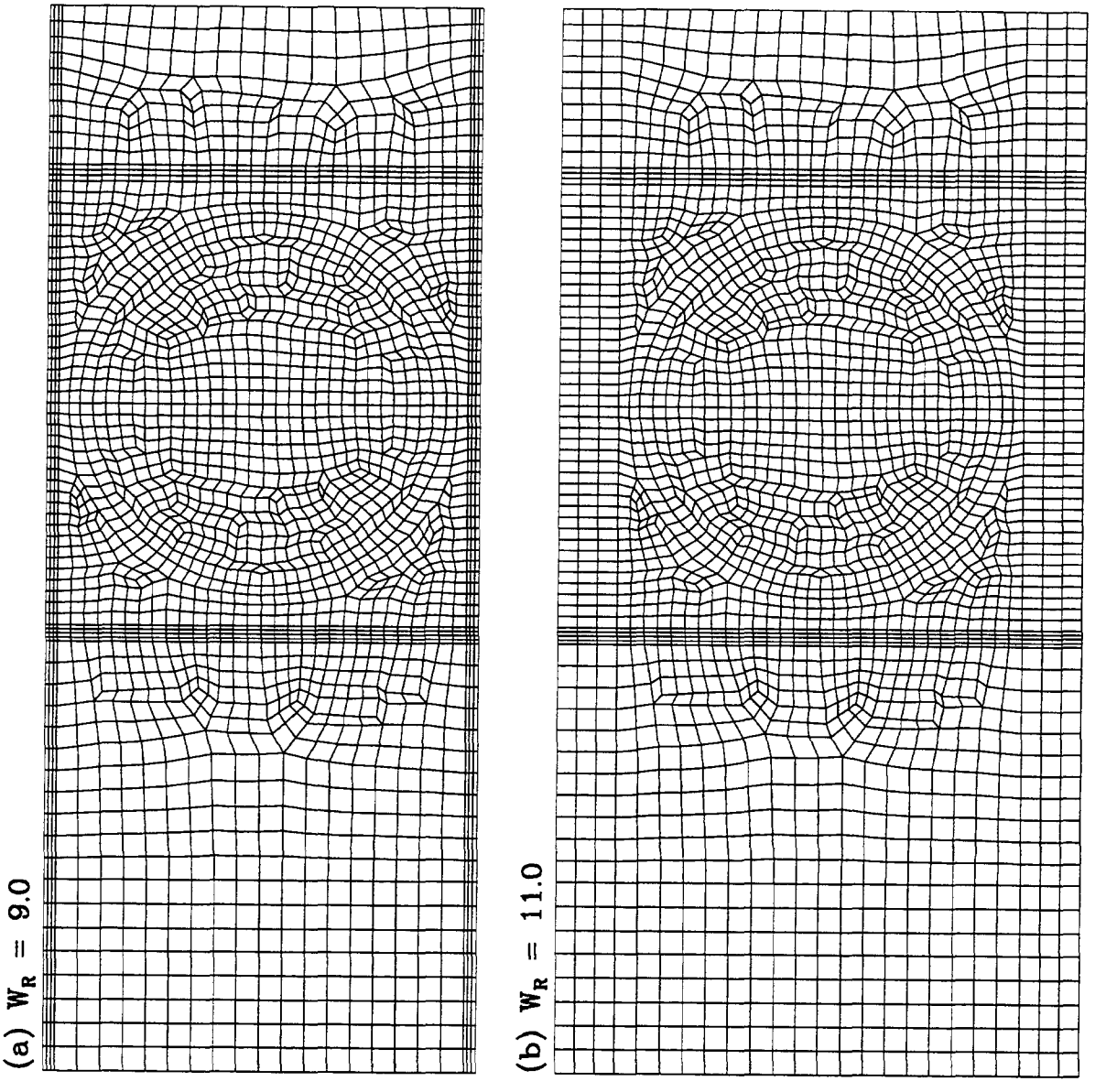

Figure 4. Results of the calculation of the deposition rate at the standard conditions listed in Table 3. The time-averaged deposition profile over the disk as a function of radial position shows a 6% faster deposition rate at the center of the disk than at the edge (6.03 vs. 5.68 Angstroms/sec) . The instantaneous deposition contours over the entire susceptor show that the decreased deposition at the edge is due to boundary layers developing from the side walls. The think contours are at 1 Angstrom/sec intervals, the thin contours at an interval of 0.25.

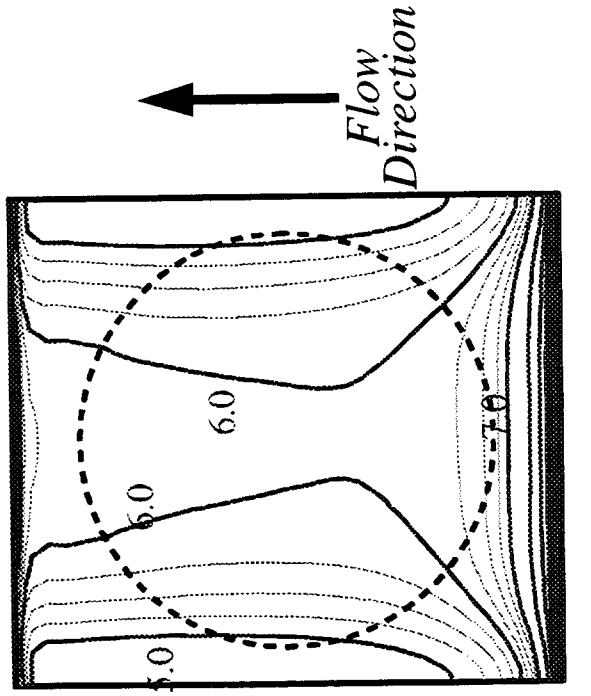

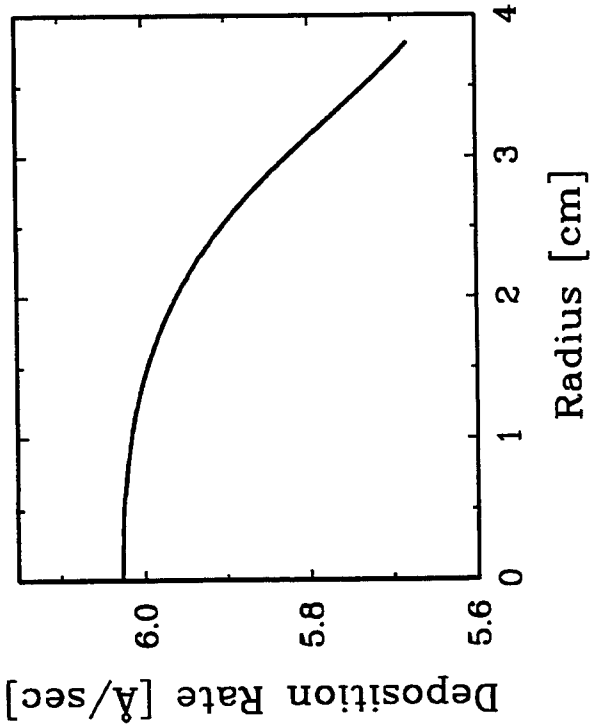

Figure 5. The results of a parameter study showing the effect of the disk spin rate, Ω, are shown. Continuation in this parameter from 0–500 rpm shows a monotonic increase in non-uniformity with Ω. The radial deposition profiles show that the increase in non-uniformity is due to increased deposition near the center of the disk. Three contour plots of the instantaneous deposition rates over the disk and surrounding susceptor show the increasing asymmetry of the deposition profiles at higher spin rates.

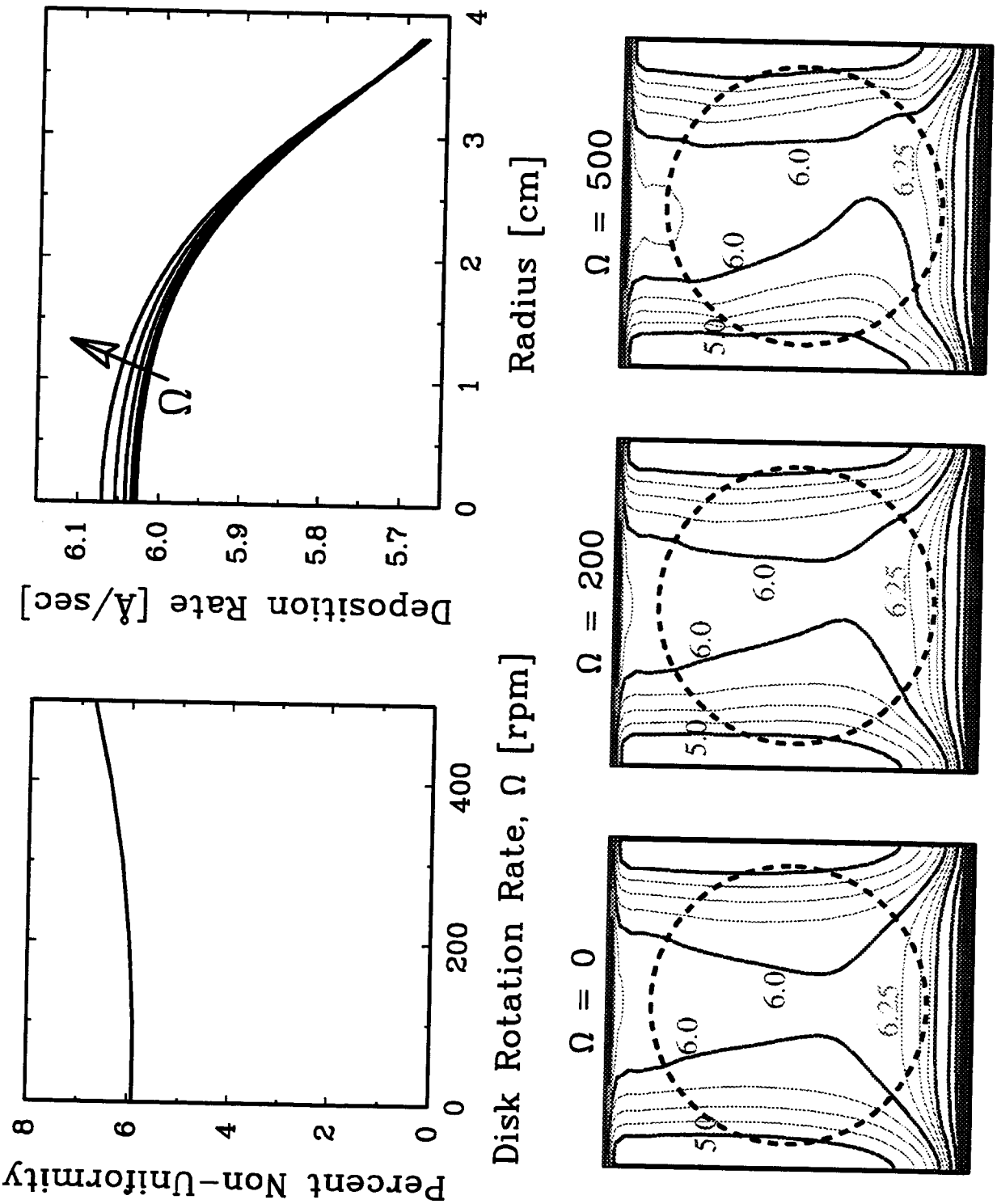

Figure 6. The results of a parameter study showing the effect of the inlet mole fraction of TMG, X, are shown. Continuation in this parameter from $0.0005 - 0.0020$ shows a slight decrease in non-uniformity with X. The radial deposition profiles show that the growth rate is highly dependent on this parameter. Three contour plots of the instantaneous deposition rates over the disk and surrounding susceptor show how the deposition rate varies linearly with X.

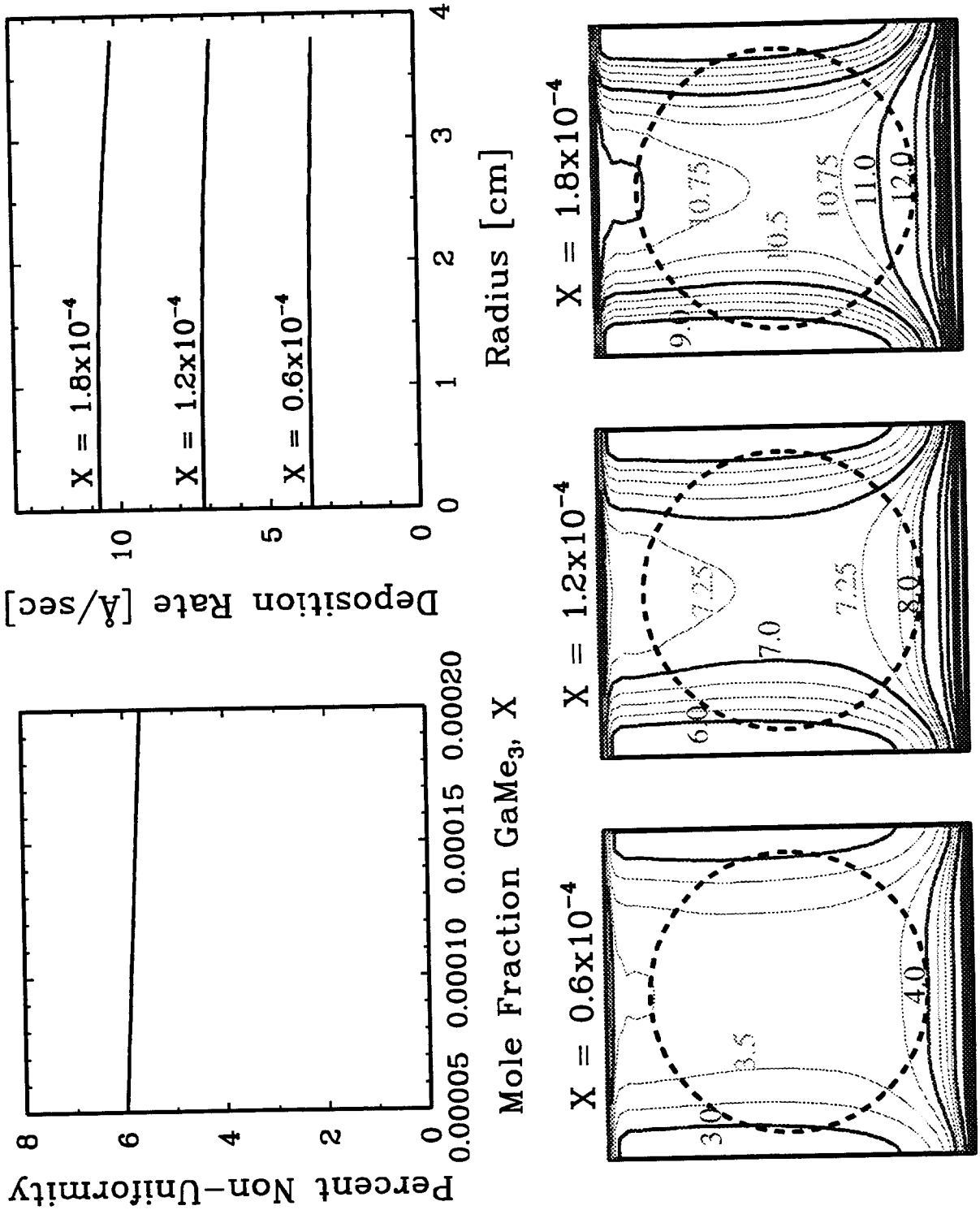

Figure 7. The results of a parameter study showing the effect of the inlet velocity, V, are shown. Continuation in this parameter from $10 - 100$ cm/sec shows a minimum near a flow rate of 68. The radial deposition profiles show that an increase in V accelerate the deposition rate on the outside of the disk faster than near the center. Three contour plots of the instantaneous deposition rates over the disk and surrounding susceptor show that this is in part due to a decrease in the boundary layers that emanate from the side walls.

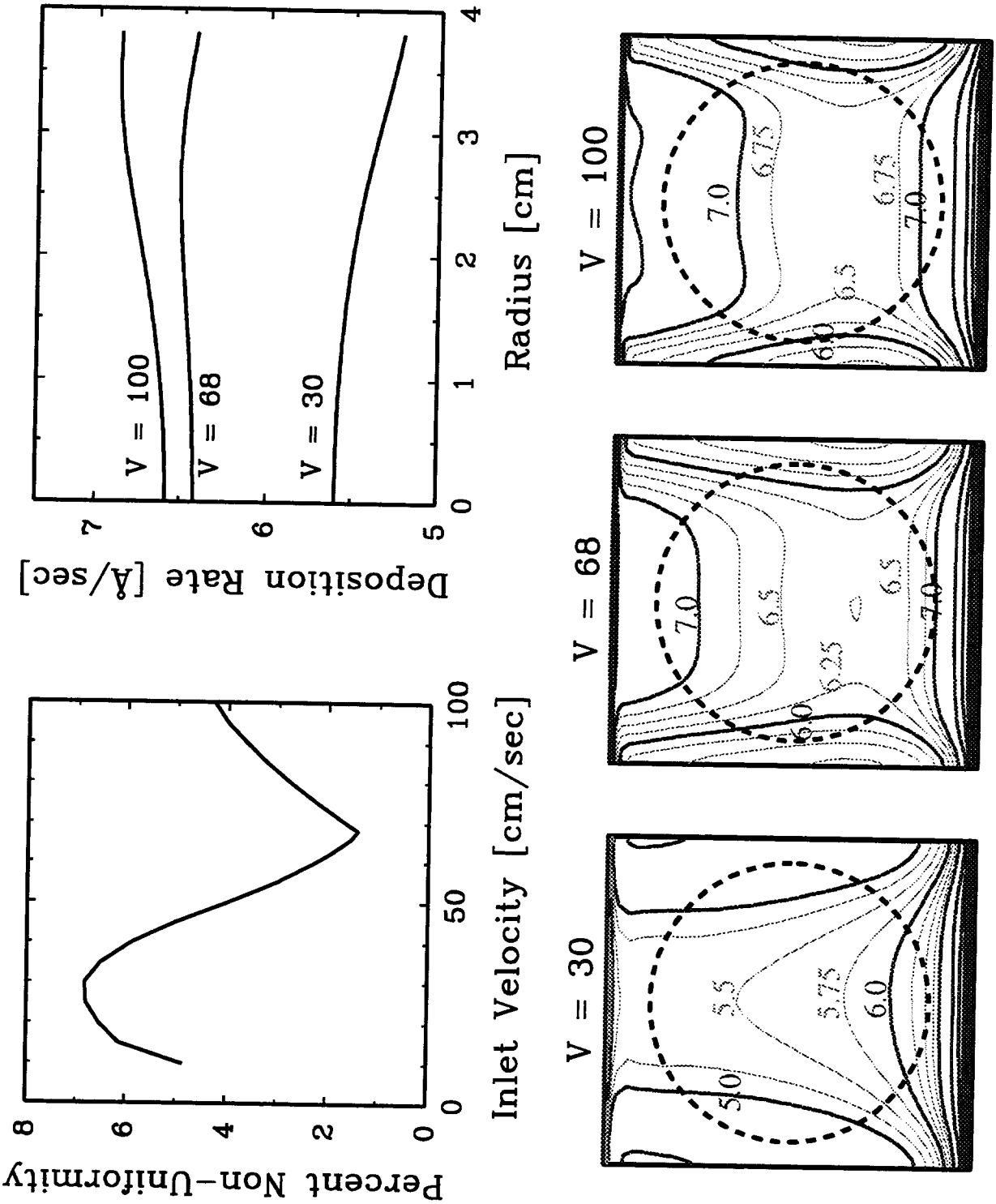

Figure 8. The results of a parameter study showing the effect of the tilt fraction, T_R, are shown. Continuation in this parameter from $0.0 - 0.95$ shows the most uniform growth at the highest degree of tilt. The radial deposition profiles show how T_R significantly effects the growth rate, but does not give insight into how T_R effects uniformity. Three contour plots of the instantaneous deposition rates over the disk and surrounding susceptor show that the improved uniformity is due to an increase in deposition at the back of the disk, which is balanced by the rotation of the disk with the lower deposition rate at the sides of the disk.

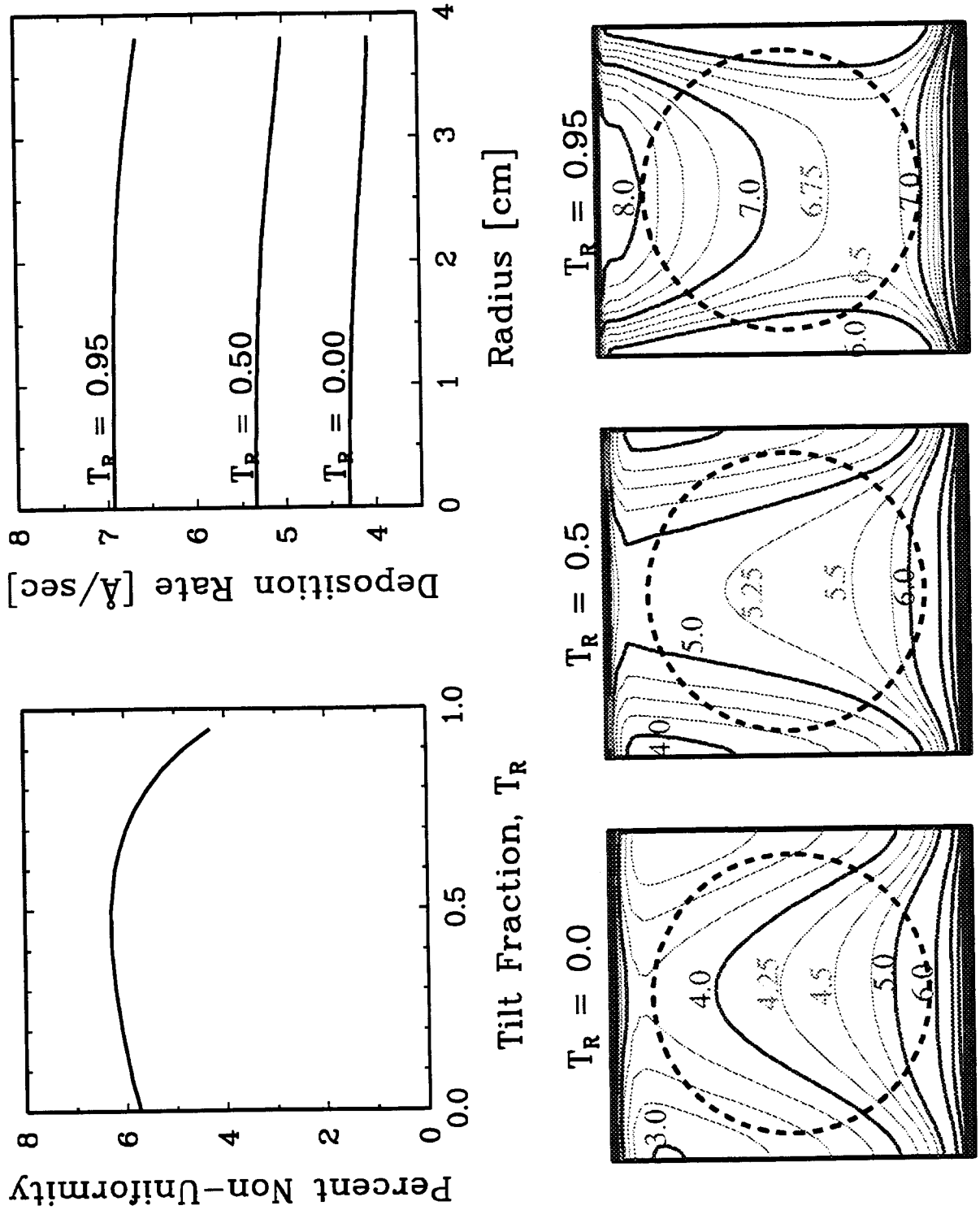

Figure 9. The results of a parameter study showing the effect of the reactor width, W_R, are shown. Continuation in this parameter from $8.7 - 13.0$ cm shows that excellent uniformity can be achieved at widths near 11.3. The radial deposition profiles show that W_R can change the convexity of the deposition rate. Three contour plots of the instantaneous deposition rates over the disk and surrounding susceptor show how an increase in width makes the effects of the boundary layers that emanate from the side walls negligible.

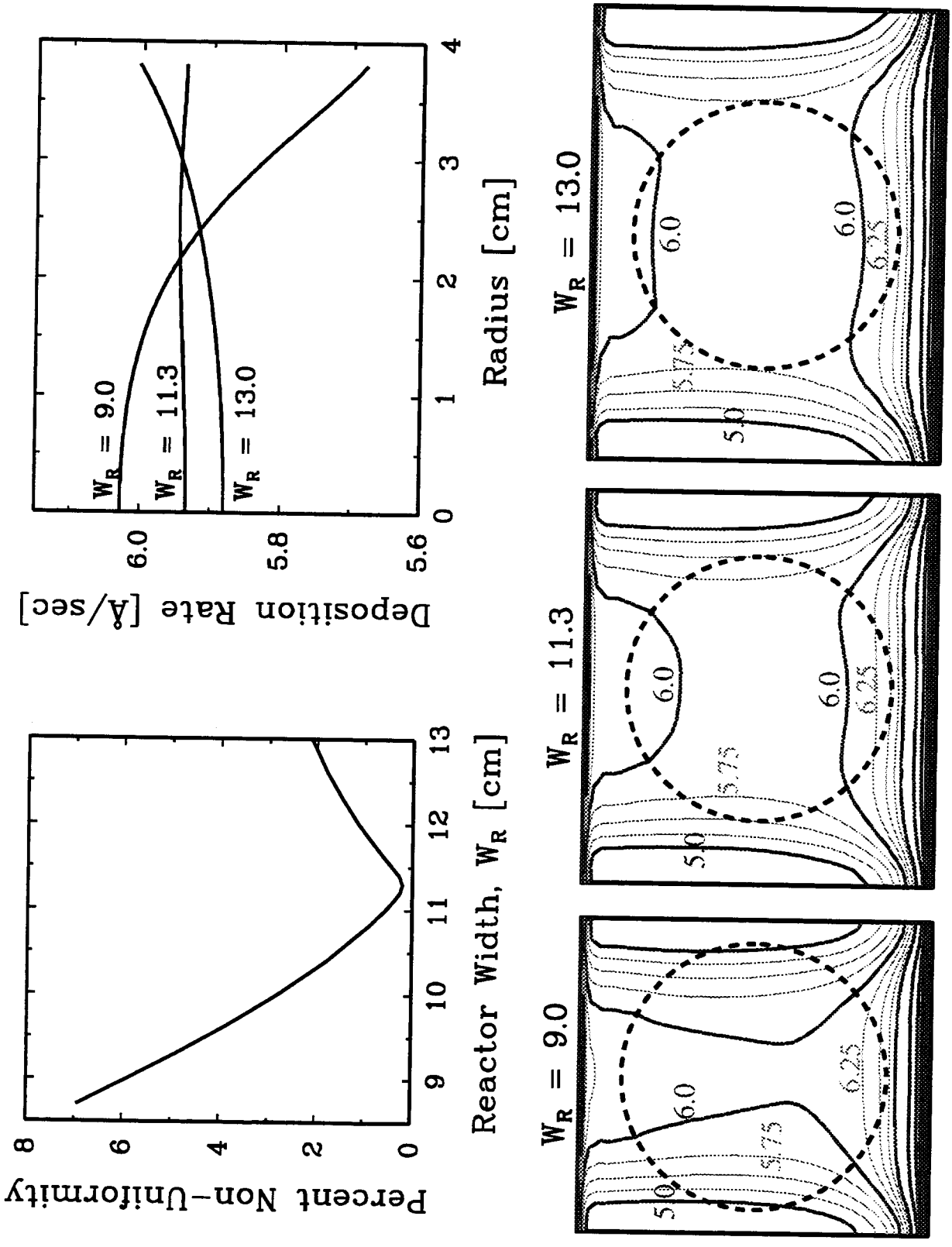

EXTERNAL DISTRIBUTION:

Rich A. Cairncross
Department of Chemical Engineering
Drexel University
Philadelphia, PA 19104

G. F. Carey
ASE/EM Dept., WRW 305
University of Texas
Austin, TX, 78712

Vernon Cole
Equipment Simulation Group, APRDL
3501 Ed Bluestein Boulevard, MD: K-10
Austin, TX 78721

Dan Coronell
Equipment Simulation Group, APRDL
3501 Ed Bluestein Boulevard, MD: K-10
Austin, TX 78721

Kevin Davis
Reaction Engineering International
77 West 200 South Suite 210
Salt Lake City, Utah 84101

Jeffrey J. Derby
Dept. of Chemical Eng. and Materials Science
University of Minnesota
421 Washington Ave. S.E.
Minneapolis, MN 55455

Yusheng Feng
Equipment Simulation Group, APRDL
3501 Ed Bluestein Boulevard, MD: K-10
Austin, TX 78721

J. E. Flaherty
Computer Science Dept.
Rensselaer Polytechnic Inst.
Troy, NY 12180

Paul Giguere
Group TSA-8
MS K575
Los Alamos National Laboratory
Los Alamos, NM 87545

R. J. Goldstein
Mechanical Engineering Department
University of Minnesota
111 Church St.
Minneapolis, MN 55455

R. Greif
Mechanical Engineering Department
6107 Etcheverry Hall
University of California
Berkeley, CA 94720-1740

Mike Heroux
Cray Research Park
655F Lone Oak Drive
Eagan, MN 55121

Dan Hitchcock
US Department of Energy
SCS, ER-30 GTN
Washington, DC 20585

Fred Howes
US Department of Energy
OSC, ER-30, GTN
Washington, DC 20585

Michael K. Jensen
Rensselaer Polytechnic Institute
Troy, NY 12180-3590

Klavs J. Jensen
Massachusetts Institute of Technology
Dept. Chem. Eng. MIT 66-566
Cambridge, Mass. 02139-4307

David Klipstein
Reaction Design
11436 Sorrento Valley Road
San Diego, CA 92121

T.J. Mountziaris
Department of Chemical Engineering
303 Furnas Hall
State University of New York
Buffalo, NY 14260-4200

S. V. Patankar
Mechanical Engineering Department
University of Minnesota
111 Church St.
Minneapolis, MN 55455

Todd Salamon
Rm. 7D-212
Lucent Technologies
600 Mountain Avenue
Murray Hill, NJ 07974

Jeffrey Scroggs
Department of Mathematics
North Carolina State University
Box 8205
Raleigh, NC 27695-8205

Farzin Shakib
ACUSIM SOFTWARE, INC.
14395 Saratoga Ave., Suite 120
Saratoga, CA 95070

T. W. Simon
Mechanical Engineering Department
University of Minnesota
111 Church St.
Minneapolis, MN 55455

Tyler Thompson
The Dow Chemical Company
External Technology / Cooperative Research
Building 1801
Midland, MI 48674-1801

Max Tirtowidjojo
DOW Chemical, Engineering Sciences
2301 N. Brazosport Blvd., B-1226
Frreport, TX 77541-3257

Dionisios Vlachos
Chemical Engineering Department
University of Massachusetts Amherst
159 Goessmann Lab, Box 33110
Amherst MA 01003-3110

David West
DOW Chemical, Engineering Sciences
2301 N. Brazosport Blvd., B-1226
Frreport, TX 77541-3257

Colin Wolden
Chemical Engineering and Pet. Ref. Department
Colorado School of Mines
P.O. Box 4028
Golden CO 80401-1887

INTERNAL DISTRIBUTION:

1	MS 0151	Gerold Yonas, 9000
1	MS 0321	William Camp, 9200
1	MS 0601	Jeff Tsao, 1126
10	MS 0601	Harry K. Moffat, 1126
1	MS 0601	M. E. Coltrin, 1126
1	MS 1111	Sudip Dosanjh, 9221
1	MS 1111	Scott Hutchinson, 9221
10	MS 1111	John N. Shadid, 9221
20	MS 1111	Andrew G. Salinger, 9221
1	MS 1111	Gary L. Hennigan, 9221
1	MS 1111	Rod C. Schmidt 9221
1	MS 1111	Matt St. John, 9921
1	MS 1111	Joe Castro, 9921
1	MS 1110	Ray S. Tuminaro, 9222
1	MS 1111	Karen Devine, 9226
1	MS 1111	Robert W. Leland, 9226
1	MS 0819	James S. Perry, 9231
1	MS 0819	Allem C. Robinson, 9231
1	MS 0841	P. L. Hommert, 9100
1	MS 0833	Johnny H. Biffle, 9103
1	MS 0316	E. D. Gorham, 9209
1	MS 0843	A. C. Ratzel, 9112
1	MS 0834	M. R. Baer, 9112
1	MS 0834	A. S. Geller, 9112
1	MS 0834	R. R. Torczynski, 9112
1	MS 0826	W. L. Hermina, 1553
1	MS 0826	T. J. Bartel, 9153
1	MS 0825	C. C. Wong, 9154
1	MS 0827	Randy Schunk, 9111
1	MS 0827	Phil Sackinger, 9111
1	MS 0827	Mario Martinez, 9111
1	MS 0827	Mike Glass, 9111
1	MS 0827	Polly Hopkins, 9111
1	MS 0827	Jim Schutt, 9111
1	MS 0827	Steve Kempka, 9111
1	MS 0834	Robert B. Campbell, 9112
1	MS 0835	Roy E. Hogan Jr., 9111
1	MS 0819	Mark A. Christon, 9231
1	MS 0826	Robert J. Cochran, 9114
1	MS 9042	Joseph F. Grcar, 8345
1	MS 9042	Chris Moen, 8345
1	MS 9042	Fran Rupley, 8345
1	MS 9042	S. K. Griffiths, 8345
1	MS 9042	Greg Evans, 8345
1	MS 9042	Bill Houf, 8345
1	MS 9042	Aili Ting, 8345
1	MS 9042	Ellen Meeks, 8345
1	MS 9042	W. Winters, 8345
1	MS 9051	Habib Najm, 8351
1	MS 9052	Mark Allendorf, 8361
1	MS 9018	Central Technical Files, 8940-2
5	MS 0899	Technical Library, 4916
2	MS 0619	Review & Approval Desk, 12690 For DOE/OSTI